



Unsupervised inter-frame motion correction for whole-body dynamic PET using convolutional long short-term memory in a convolutional neural network

Xueqi Guo^a, Bo Zhou^a, David Pigg^b, Bruce Spottiswoode^b, Michael E. Casey^b, Chi Liu^{a,c,*}, Nicha C. Dvornek^{a,c,*}

^aDepartment of Biomedical Engineering, Yale University, New Haven, CT 06511, USA

^bSiemens Medical Solutions USA, Inc., Knoxville, TN, 37932, USA

^cDepartment of Radiology and Biomedical Imaging, Yale University, New Haven, CT 06511, USA

ARTICLE INFO

Article history:

Received DD MM 2021

Keywords: convolutional network, long-short term memory, motion correction, parametric imaging, whole-body dynamic PET

ABSTRACT

Subject motion in whole-body dynamic PET introduces inter-frame mismatch and seriously impacts parametric imaging. Traditional non-rigid registration methods are generally computationally intense and time-consuming. Deep learning approaches are promising in achieving high accuracy with fast speed, but have yet been investigated with consideration for tracer distribution changes or in the whole-body scope. In this work, we developed an unsupervised automatic deep learning-based framework to correct inter-frame body motion. The motion estimation network is a convolutional neural network with a combined convolutional long short-term memory layer, fully utilizing dynamic temporal features and spatial information. Our dataset contains 27 subjects each under a 90-min FDG whole-body dynamic PET scan. With 9-fold cross-validation, compared with both traditional and deep learning baselines, we demonstrated that the proposed network obtained superior performance in enhanced qualitative and quantitative spatial alignment between parametric K_i and V_b images and in significantly reduced parametric fitting error. We also showed the potential of the proposed motion correction method for impacting downstream analysis of the estimated parametric images, improving the ability to distinguish malignant from benign hypermetabolic regions of interest. Once trained, the motion estimation inference time of our proposed network was around 460 times faster than the conventional registration baseline, showing its potential to be easily applied in clinical settings.

© 2022 Elsevier B. V. All rights reserved.

1. Introduction

Whole-body positron emission tomography (PET) has been used in clinical and research protocols as a quantitative physiologic measurement primarily for oncological applications (Ziegler, 2005). Static 2-deoxy-2-[¹⁸F]fluoro-D-glucose (FDG) imaging is a commonly applied measurement for tumor glycolytic metabolism and energy consumption (Muzi et al., 2012), but semi-quantitative measurement from static PET is generally

considered inferior to quantitative parameter estimation from dynamic PET, since the radiotracer uptake is a time-dependent process determined by various physiological factors (Karakatsanis et al., 2013); (Dimitrakopoulou-Strauss et al., 2021). In dynamic PET with continuous-bed-motion mode (CBM), an image sequence with multiple frames is acquired over 90-120 minutes starting from the radiotracer injection, and voxel-by-voxel tracer kinetic modeling is applied to generate parametric images (Gallezot et al., 2019). The Patlak slope K_i , the net uptake rate constant, has been reported with superior tumor-to-background and contrast-to-noise ratio in oncologic lesion detection as compared to static PET imaging (Fahrni et al., 2019).

*Corresponding author. Email: nicha.dvornek@yale.edu, chi.liu@yale.edu

However, the unavoidable patient motion during the long acquisition time of whole-body dynamic PET can seriously impact parametric imaging. Typically, patient motion can be further divided into respiratory motion, cardiac motion, and body motion. The intra-frame respiratory and cardiac motion introduces blurring to reconstructed image and degrades the image resolution. The inter-frame mismatch can originate from voluntary body movement and the long-term respiratory and cardiac motion pattern change, subsequently introducing attenuation correction artifacts and increasing errors in parameter estimation (Lu et al., 2019). Due to the non-rigid, complex, and unpredictable nature of patient motion, the inter-frame motion correction problem still remains challenging. Additionally, substantial tracer distribution change occurs across the dynamic frames, causing further challenges in motion estimation and correction.

Recently proposed motion correction methods for PET typically utilize external motion tracking systems, data-driven motion estimation algorithms, or traditional non-rigid registration methods. Real-time motion tracking hardware has been investigated for respiratory and head motion compensation (Lu et al., 2018; Noonan et al., 2015), but requires extra setup time. Data-driven joint motion estimation and correction frameworks without additional devices are preferred, which have been investigated for brain (Lu et al., 2020), respiratory (Feng et al., 2017), and body motion (Lu et al., 2019). However, these approaches have not yet been fully explored in dynamic PET, which requires taking the rapidly changing radiotracer distribution into consideration. We have previously reported that traditional non-rigid registration could successfully correct the inter-frame misalignment (Guo et al., 2021) through the entropy-based multi-resolution approach in BioImage Suite (BIS) (Joshi et al., 2011), but the optimization process is often computationally intensive and may not be feasible in clinical translation.

Deep learning has achieved promising performance in medical image processing and analysis tasks. Convolutional neural networks (CNNs) can extract local information in images and has been widely applied in image registration. Popular baseline models include Quicksilver (Yang et al., 2017) and Voxel-morph (Balakrishnan et al., 2019), and both have been successfully implemented for brain MR image registration. However, these CNN models consider only a single image pair without distinct tracer kinetics, which could be a barrier for dynamic PET. Temporal models like recurrent neural networks (RNN) (Medsger and Jain, 2001), including the popular long short-term memory (LSTM) networks (Hochreiter and Schmidhuber, 1997), have been successfully applied on sequential data analysis tasks such as language modeling (Merity et al., 2017). In medical applications, LSTM models have been developed for cardio-respiratory motion prediction (Azizmohammadi et al., 2019) and real-time liver tracking (Wang et al., 2021a), but these works mainly focused on 1-D motion patterns. An LSTM spatial co-transformer was proposed for fetal ultrasound and magnetic resonance image registration, but was still limited to rigid motion (Wright et al., 2018). In combination with a CNN, the RNN and LSTM have been successfully applied in cardiac analysis such as echocardiographic assessment (Abdi

et al., 2017), automatic interpretation (Huang et al., 2017), and full left ventricle quantification (Xue et al., 2018).

Convolutional LSTM networks (Shi et al., 2015) were designed to simultaneously extract and leverage both temporal and spatial information. For video or dynamic medical image processing with 2-D or 3-D spatial features in addition to the temporal information, the combination of CNN and convolutional LSTM networks has been shown to extract spatial-temporal information effectively. In gesture and action recognition, improved accuracy and robustness were reported using a 3-D CNN with convolutional LSTM (Zhu et al., 2017; Ge et al., 2019). A spatiotemporal encoder architecture followed by a convolutional LSTM was proposed for video violence detection, gaining better performance on the heterogeneous datasets (Hanson et al., 2018). In medical image applications, this combination also achieved superior performance. The cascaded convolutional LSTM layers after a CNN block achieved higher dice similarity and F-1 score in 3-D electron microscopic (Chen et al., 2016) and cardiac MR (Zhang et al., 2018b) image segmentation. A model with a CNN and combined multiple convolutional LSTM layers was proposed for non-linear 3-D MRI-transrectal ultrasound image registration, achieving well-aligned landmarks (Zeng et al., 2020).

In addition to the simple concatenation following a CNN, the convolutional LSTM layer has also been used as a replacement or modification of the layers in popular CNN architectures, such as the U-Net (Ronneberger et al., 2015). The structure of using convolutional LSTM layers as the encoding layers of a U-Net has been proposed for change detection in remote sensing (Sun et al., 2020) and satellite images (Papadomanolaki et al., 2021), and for microscopy cell segmentation (Arbelle and Raviv, 2019). The replacement of the feature map concatenations using a convolutional LSTM layer has been implemented on multimodal medical image segmentation tasks (Zhang et al., 2018a; Azad et al., 2019). However, such combination of convolutional LSTMs with the U-net structure have yet to be fully investigated in image registration.

In dynamic PET imaging, the application of CNN-LSTM models is still nascent. To guide the selection of an optimal motion correction method for dynamic PET, a CNN-LSTM classifier was built to characterize regular and irregular breathing patterns from respiratory traces collected by an external system (Guo et al., 2019). An automated CNN-LSTM motion correction framework was implemented for cardiac dynamic PET (Shi et al., 2021), but considered only rigid translation motion under simulation. A joint motion correction and denoising network was proposed with a siamese pyramid network and a bidirectional convolutional LSTM layer for low-dose gated PET (Zhou et al., 2021), but focused mainly on respiratory motion. Under the whole-body scope, deep learning based inter-frame motion correction for dynamic PET still remains unexplored.

In this work, we developed a deep learning framework for unsupervised inter-frame motion correction in whole-body dynamic PET. The proposed motion estimation network is a deep CNN with an integrated convolutional LSTM layer at the bottleneck of a U-net-like architecture to capture both temporal tracer kinetics information and local spatial features simultaneously.

Table 1. Demographic characteristics of the included subjects (mean \pm standard deviation, range)

Demographic	Unit	Statistics
Age	year	56 \pm 14 (24 - 77)
Body mass index	kg/m ²	28.2 \pm 3.9 (21.6 - 37.2)
Plasma glucose	mg/dL	101.36 \pm 16.76 (75.33 - 142.00)
FDG injection	mCi	9.04 \pm 0.88 (6.91 - 10.28)

A spatial transform layer then warps the frames according to the estimated displacement fields. We comprehensively evaluated the model performance using 9-fold cross-validation on a real patient dataset by qualitative and quantitative metrics in parametric imaging, with comparisons to both traditional and other deep learning-based registration methods. Finally, we demonstrated the potential for impacting downstream analysis of the parametric images through the classification of malignant and benign hypermetabolic regions of interest.

2. Material and methods

2.1. Dataset

A total of 27 anonymized human subjects (5 healthy and 22 cancer patients) were included from January 2017 to February 2020 at the Yale PET center, with obtained informed consent from all the subjects and approval by the Yale Institutional Review Board. Table 1 summarizes the demographic characteristics of the included subjects.

Each subject undertook a 90-min dynamic whole-body FDG CBM PET scan on a Biograph mCT PET/CT (Siemens Healthineers) with a weight-based bolus FDG injection (Naganawa et al., 2020). A non-contrast CT scan was acquired for attenuation correction prior to the tracer injection. In the first 6 minutes, a single-bed scan over the heart acquired 9 frames (6 \times 0.5 min and 3 \times 1 min) for each subject. Nineteen consecutive CBM whole-body frames were then captured (4 \times 2 min and 15 \times 5 min) under typewriter mode, with the bed movement always from superior to inferior and a fast shift back in each frame interval. The intra-frame bed movement speed was steady but subject-dependent as taller subjects would require faster bed motion. In 22 of 27 subjects, sequential arterial blood samples were collected and counted for plasma activity measurements. For the remaining 5 of 27 subjects, the normalized population based input function was used in parametric fitting.

All the dynamic frames were reconstructed by the ordered subsets expectation maximization (OSEM) algorithm (Hudson and Larkin, 1994) with 21 subsets and 2 iterations on the scanner. Attenuation, scatter, randoms, normalization, and decay corrections (Panin et al., 2014) as well as a 5-mm Gaussian smoothing filter were applied to the quantitative image reconstruction following our standard clinical protocol. The voxel size of the reconstructed images was 2.04 \times 2.04 \times 2.03 mm³ for all the subjects, with the image matrix size of 400 \times 400 in the transverse plane and between 489 and 859 slices per 3D whole-body frame as taller patients have more slices. 57 hypermetabolic regions of interest (ROIs) (8 benign and 49 ma-

lignant) were selected in the 22 cancer subjects by a nuclear medicine physician for further motion correction evaluation.

2.2. Network architecture

In Figure 1, the overall workflow of the multiple-frame motion correction network is displayed. The input of the network is a dynamic frame sequence, each paired with the reference frame. With the estimated displacement fields, the following spatial transformation layer warps the original frames and get the motion compensated frames as the outputs. As in Eq. 1, the loss function of the model contains an image similarity measurement using normalized cross correlation (NCC) as well as a regularization term of the local discontinuity of the displacement fields,

$$\mathcal{L} = \sum_{j=1}^M -NCC(F_R, \widehat{F}_{Mj}) + \lambda |\nabla \phi_j|^2, \quad (1)$$

where F_R is the reference frame, \widehat{F}_{Mj} is the j^{th} warped moving frame, λ is the regularization factor, and ϕ_j is the estimated displacement field of the j^{th} frame. The NCC similarity is superior to mean squared error when taking the rapidly changing tracer distribution across the dynamic frames into consideration, and was also shown to have better accuracy and robustness on GPU-based calculations in a previous evaluation study (Wu et al., 2009).

In order to capture the tracer distribution change along time as well as the local spatial features, the motion correction network needs to be able to handle multiple dynamic frames simultaneously. LSTMs are a special kind of recurrent neural network variant that is robust and powerful for long-term dependencies (Shi et al., 2015). Compared to fully connected LSTMs, the convolutional LSTMs enhanced the temporal feature extraction with spatial information encoded (Shi et al., 2015). The key equations in a convolutional LSTM cell are shown in Eq. 2-7, where \otimes is the convolution operator and $*$ is the element-wise product:

$$i_t = \sigma(W_i \otimes x_t + U_i \otimes h_{t-1} + b_i) \quad (2)$$

$$f_t = \sigma(W_f \otimes x_t + U_f \otimes h_{t-1} + b_f) \quad (3)$$

$$\tilde{c}_t = \tanh(W_c \otimes x_t + U_c \otimes h_{t-1} + b_c) \quad (4)$$

$$c_t = i_t * \tilde{c}_t + f_t * c_{t-1} \quad (5)$$

$$o_t = \sigma(W_o \otimes x_t + U_o \otimes h_{t-1} + b_o) \quad (6)$$

$$h_t = o_t * \tanh(c_t) \quad (7)$$

At the time point t , x_t is the sequence input, c_t is the cell state, \tilde{c}_t is the estimated cell state, c_{t-1} is the cell state at the previous time point ($t-1$), h_t is the hidden state, and h_{t-1} is the previous hidden state. i_t is the input gate (Eq. 2) that decides whether the information from the current input will be updated to \tilde{c}_t . f_t is the forget gate (Eq. 3) that determines what information from c_{t-1} will be kept. The current cell state is first estimated with the current input and the previous hidden state (Eq. 4). Then, to update the cell state (Eq. 5), the current estimation and the previous cell state will be combined with restrictions from the

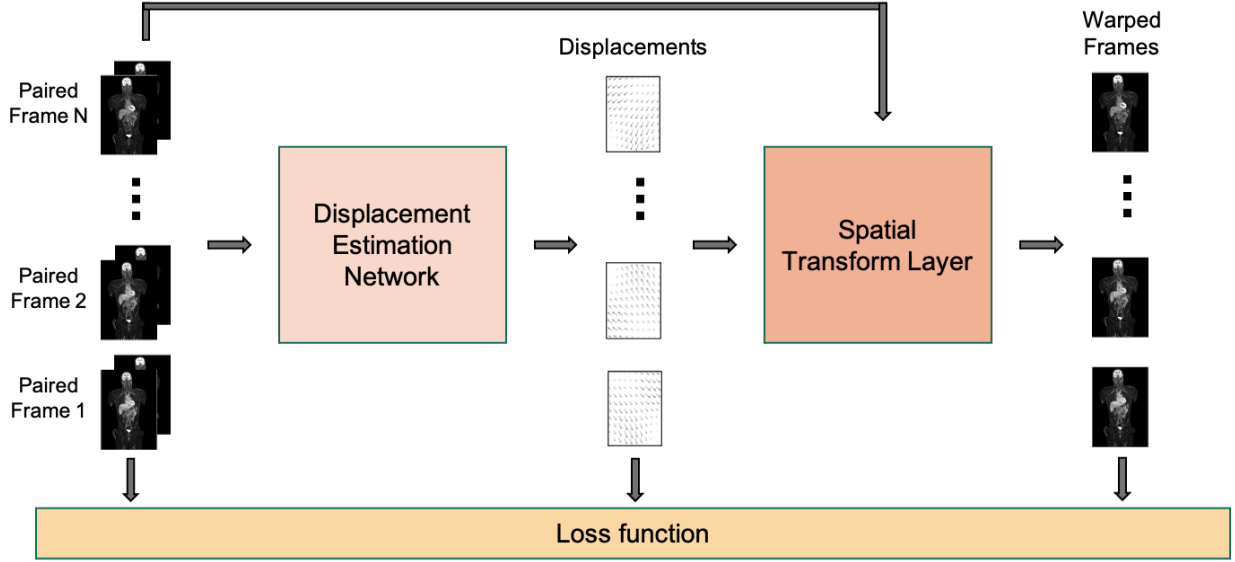


Fig. 1. The overall workflow of the multiple-frame motion correction framework. Each paired frame is the i^{th} moving frame with the reference frame.

input and forget gates respectively. Finally, the cell state is multiplied with the output gate (Eq. 6) to get the hidden state (Eq. 7), which is the LSTM cell output. W and U matrices contain weights applied to the current input and the previous hidden state, respectively, b vectors are the biases for each layer, and σ represents the sigmoid function. In a conventional LSTM cell, the key equations are similar to a convolutional LSTM cell except all the input-to-state and state-to-state transitions are fully connected.

Our proposed displacement estimation network is shown in Figure 2. We developed a convolutional motion estimation network architecture with an integrated convolutional LSTM layer, with the ability to detect and analyze multiple frames simultaneously. The spatial-temporal structure allows the network to capture the cross-frame information from not only the adjacent frames but also non-adjacent frames, especially for the long-duration motion that could affect multiple frames. In addition, capturing the inter-frame kinetic tracer distribution change can also potentially improve motion estimation accuracy. The CNN structure is similar to a 3-D U-Net (Çiçek et al., 2016) with 4 encoding and decoding levels (Balakrishnan et al., 2019) and input sequence length $N = 5$. In each level, the 3-D convolutional layer has kernel size of $3 \times 3 \times 3$, with 16 kernels for the first layer and 32 kernels for the following ones. The convolutional LSTM layer is combined at the bottleneck of the 3-D U-Net to process the encoded spatial-temporal features, with 32 kernels in the size of $3 \times 3 \times 3$.

2.3. Model training and comparison

The inter-frame motion correction was applied to all the 5-min frames (Frame 5 - Frame 19) with Frame 12 as the reference frame. Five consecutive frames from the same subject are sent into the network at one time as the data augmentation in the temporal dimension. The input frames were downsampled by a factor of 4 and zero-padded to the same resolution of $128 \times 128 \times 256$. All dynamic frames were converted to standardized

uptake values (SUV) units prior to the network input. We implemented an intensity cutoff at $SUV = 2.5$ with Gaussian noise ($\sigma = 0.01$) added to the thresholded voxels only for displacement computation but not the final images. The intensity cutoff is intended to mitigate the driving force from the high-intensity bladder voxels, and the added Gaussian noise helps avoid local saturation in the local NCC computation. The output displacement fields were then upsampled to the original resolution before warping the original frames.

We compared our proposed model to both traditional and deep learning motion correction baselines under the same intensity cutoff implementation. The traditional entropy-based non-rigid registration is implemented in BIS (Joshi et al., 2011), with both original and downsampled resolution images. The entropy-based normalized mutual information was chosen as the similarity measure of BIS to support the changing tracer distribution in dynamic PET with robustness in CPU-based calculations (Wu et al., 2009). The optimization was conducted for two resolution levels with the final resolution at one half of the original resolution and step size as 2.0. The control point spacing of the free-form deformations was 50.0 mm with a spacing rate of 1.1 for lower resolution levels. All the other registration parameters in BioImage Suite were set as the default. The Voxelmorph framework (Balakrishnan et al., 2019) is selected as the deep learning image registration baseline. We implemented both single pairwise registration as in the original Voxelmorph framework and a variant using multiple-frame input to compare the performance difference between sequential input considering only more registration pairs and the temporal LSTM layer. In addition to the proposed convolutional LSTM combined at the U-Net bottleneck (B-convLSTM), we further tested two other variants: using a fully connected LSTM layer at the bottleneck (B-LSTM) to test the difference between dense and convolutional LSTM cells, and the serial implementation of the convolutional LSTM following the U-Net output (S-convLSTM) as comparison to the most common approach

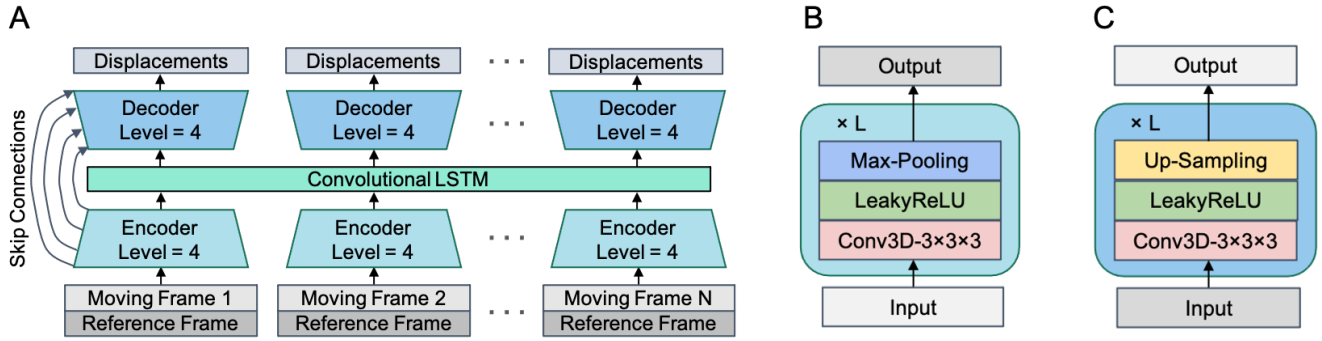


Fig. 2. The proposed displacement estimation network. (A) The network structure; (B) A single encoder level; (C) A single decoder level.

to combining CNNs with convolution LSTMs.

All the deep learning frameworks were implemented using Keras and TensorFlow backend and trained on a NVIDIA Quadro RTX 8000 GPU. The same downsampling strategy was applied to all the deep learning based models. The stopping epoch was chosen based on the observations of reaching the minimum validation loss, which was 750 for single pairwise Voxelmorph while that of all the multiple frame models was 500. All the networks are trained using the Adam optimizer (learning rate = 10^{-4}) with batch size = 1, the same loss function, and the regularization factor $\lambda = 1$.

2.4. Parametric imaging and evaluation metrics

The Patlak plot technique was used to analyze tracer pharmacokinetics (Patlak et al., 1983). As shown in Eq. 8, the Patlak plot was fitted voxel-wise with the dynamic frames and the input function after a starting time $t^* = 20$ min (Ye et al., 2018; Toczek et al., 2020),

$$C_T(t) = K_i \int_0^t C_P(\tau) d\tau + V_b C_P(t) \quad (8)$$

where C_T is the tissue tracer concentration, C_P is the plasma tracer concentration (input function), the slope K_i is the net uptake rate constant, and the y-axis intercept V_b is the distribution volume. This approach more easily introduces image-based regression weights to the estimation process (Carson, 2005).

The K_i and V_b images were overlaid to qualitatively visualize any motion-related mismatch. K_i and V_b are sensitive to body motion (Lu et al., 2019), where K_i is more heavily affected by later frames while V_b is more impacted by earlier frames. Thus, better alignment of K_i and V_b images signifies improved registration across the dynamic frames. The whole-body normalized mutual information (NMI) as well as the whole-body NCC between K_i and V_b images were computed as the quantitative measurement for the alignment.

As shown in Eq. 9, the normalized weighted mean fitting errors (NFE) were computed to quantitatively assess the disparity between the dynamic data and the fitted results,

$$NFE = \frac{\sum_{k=1}^n w_k (\widehat{C_T}(t_k) - C_T(t_k))^2}{(k-2) \sum_{k=1}^n \left(\frac{w_k C_T(t_k)}{n} \right)^2} \quad (9)$$

where w_k is the time activity curve fitting weight after decay correction (Chen et al., 1991, 1995), $\widehat{C_T}(t_k)$ is the estimated tissue tracer concentration, $C_T(t_k)$ is the observed tissue tracer concentration, t_k represents the middle time of the k^{th} frame, and n is the number of dynamic frames after t^* . The voxel-wise NFE maps were visualized as qualitative evaluation, and the NFE statistics in the whole-body, head, and ROIs were collected for quantitative evaluation.

A 9-fold subject-wise cross-validation was implemented to comprehensively evaluate the performance of all the motion correction methods. Significant differences between quantitative measurements from different motion correction methods were assessed using paired two-tailed t-tests with $\alpha = 0.05$.

2.5. ROI analysis

We computed the mean, maximum, and the standard deviation of the K_i value for each ROI before and after each motion correction method was applied.

To assess the motion correction impact on benign/malignant classification capability, we concatenated the three reported features and trained four machine learning models for tumor classification: logistic regression (LR), linear support vector classifier (SVC), non-linear SVC with the radial basis function kernel, and random forest (RF). All the machine learning models were implemented using scikit-learn with all the default hyperparameters. As the ROI group is relatively small and imbalanced with more malignant lesions than benign ones, a 5-fold stratified cross validation was implemented with assigned sample weights inversely proportional to the benign/malignant ratio. For each machine learning model, the mean receiver operating characteristic (ROC) curve was generated from the mean of the sensitivity and specificity values for the 5 folds by varying the classification score thresholds, and the area under the curve (AUC) was then computed as the assessment of classification capability.

3. Results

3.1. Qualitative evaluations

Figure 3 shows the inter-frame motion impact and the correction effects on the overlaid Patlak K_i and V_b images. Without motion correction, the Patlak K_i and V_b overlaid images

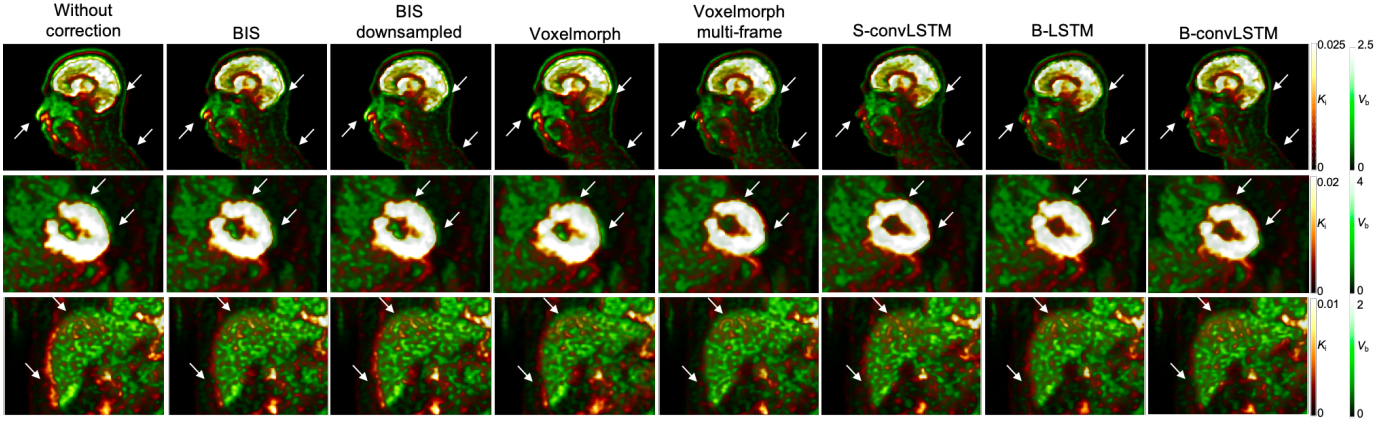


Fig. 3. Sample overlaid Patlak K_i (red) and V_b (green) images showing inter-frame motion and correction impacts in brain (upper), heart (middle), and liver (bottom).

display spatial misalignments originating from the inter-frame motion. The non-rigid method of BIS substantially reduced the misalignment at the head, heart, and liver, but under-correction existed with some remaining mismatch. The performance of BIS further degraded when operating on downsampled dynamic frames, which were the same inputs used for the deep learning approaches. The baseline model Voxelmorph with single image pair input also showed similar trends, with improved alignment but remaining mismatch as well. The multi-frame version of Voxelmorph further enhanced the K_i and V_b alignment, showing that letting the network “see” more input frames simultaneously is a key improvement in the dynamic frame registration. The results of the B-LSTM model were even better aligned, indicating the power of recurrent analysis. Finally, the two convolutional LSTM models achieved the best visual spatial alignment improvement. Specifically, the B-convLSTM model corrected the non-rigid misalignment at the lower right brain edge and the liver boundary the best, while the S-convLSTM model reduced the misalignment from the rigid motion at the nose outline and the heart boundary the most. Note that the heart underwent significant motion and all the motion correction methods changed the spatial location and the shape of the heart, with the B-convLSTM model preserving the heart shape the best. This implies that motion correction using the multi-frame input and the convolutional LSTM for extracting spatial and temporal information could enhance the qualitative spatial alignment of the parametric images.

The significant motion impact on K_i and V_b misalignment could be detected in 23 out of 27 subjects; the most commonly detected voluntary movement of the head including rigid movement of the skull and the brain deformation could be found in all of the 27 subjects. Some motion-related artifacts include the “ridge-valley” artifact (Lu et al., 2019) and the same hypermetabolic peak appearing in adjacent locations in K_i and V_b images. According to the sample figures, the proposed spatial-temporal network was able to further reduce those artifacts and improve the motion compensation as well as lead to altered K_i and V_b values, though the ground truth of the K_i and V_b values are lacking in a real patient dataset.

The sample voxel-wise NFE maps are visualized in Figure 4.

The NFE map of the proposed network was overall darker than the maps without motion correction and other motion correction baselines under the same color bar scaling, indicating further reduced fitting error in the Patlak model. The total number of hotspot voxels representing higher voxel-wise fitting errors decreased in the sample NFE map after the proposed motion correction. For the most common head motion, the proposed networks further reduced the high error peaks at the head and brain edge. For the heart region with high fitting error due to the significant motion, the proposed networks additionally diminished the hotspots in the ventricles and at the edges. Our proposed model B-convLSTM reduced the peaks and the brightness of the NFE maps the most.

3.2. Quantitative evaluations

Table 2 summarizes the quantitative evaluations of the inter-frame motion correction methods. The proposed B-convLSTM network significantly reduced mean NFE in Patlak fitting in the whole-body and subareas with significant motion (head and ROIs) and raised the quantitative K_i/V_b alignment measurements compared with traditional non-rigid and Voxelmorph baselines (all with $p < 0.05$). For the whole-body maximum NFE, the BIS methods tended to increase the peak values, with the average maximum NFE increasing by ~ 5 fold and the largest errors increasing by ~ 50 fold. In contrast, the proposed model successfully reduced both the lower and upper end of the peak error range. The B-convLSTM model achieved the lowest whole-body, head, and ROI NFE while the S-convLSTM attained the highest K_i/V_b NMI and NCC, potentially indicating that the S-convLSTM model is more sensitive to matching image noise.

The inference (wall) time of motion estimation and the model size of each motion correction method are summarized in Table 3. Note that all the deep learning models are trained under the downsampled resolution while the original BIS method used the full resolution images. Under the same downsampled resolution, the well-trained B-convLSTM model could perform motion estimation ~ 17 times faster than BIS and ~ 6 times faster than the single image pair Voxelmorph, since the multiple frame

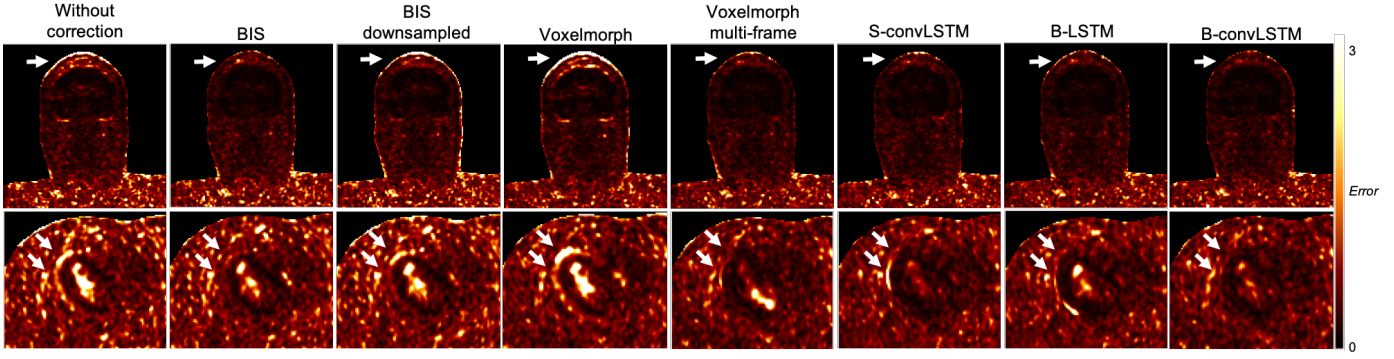


Fig. 4. Sample voxel-wise Patlak NFE maps of skull and brain (upper) and heart (bottom).

Table 2. Quantitative assessments of the inter-frame motion correction methods (mean \pm standard deviation, range)

	Whole-body mean NFE	Whole-body maximum NFE	Head NFE	ROI NFE	K_i/V_b NMI	K_i/V_b NCC
Without correction	0.1559 \pm 0.0696 (0.0716 - 0.4093)	16.1518 \pm 3.6710 (7.2930 - 22.2021)	0.1103 \pm 0.0530 (0.0495 - 0.2630)	1.3526 \pm 2.1897 (0.1831 - 15.9933)	0.9298 \pm 0.0312 (0.8567 - 0.9738)	0.2695 \pm 0.1110 (0.0503 - 0.4512)
BIS	0.1418 \pm 0.0584 (0.0686 - 0.3671)	70.1237 \pm 245.5716 (7.2911 - 1314.6486)	0.0915 \pm 0.0442 (0.0438 - 0.2479)	1.0298 \pm 1.1165 (0.1571 - 7.4314)	0.9451 \pm 0.0283 (0.8567 - 0.9794)	0.3150 \pm 0.1067 (0.1179 - 0.5354)
BIS downsampled	0.1517 \pm 0.0597 (0.0730 - 0.3725)	87.8017 \pm 245.8142 (4.7684 - 1003.5248)	0.0980 \pm 0.0446 (0.0513 - 0.2594)	1.1361 \pm 1.6262 (0.1647 - 11.8469)	0.9430 \pm 0.0248 (0.8783 - 0.9736)	0.3151 \pm 0.1007 (0.1336 - 0.5079)
Voxelmorph	0.1492 \pm 0.0640 (0.0670 - 0.3865)	15.2463 \pm 4.0112 (7.2963 - 21.9768)	0.1152 \pm 0.0463 (0.0517 - 0.2480)	1.3616 \pm 2.0005 (0.2769 - 14.4634)	0.9319 \pm 0.0303 (0.8601 - 0.9748)	0.2733 \pm 0.1109 (0.0525 - 0.4496)
Voxelmorph multi-frame	0.1181 \pm 0.0476 (0.0548 - 0.3023)	15.2255 \pm 4.0066 (3.9533 - 21.5372)	0.0801 \pm 0.0385 (0.0372 - 0.2128)	0.8949 \pm 1.1831 (0.1494 - 8.4020)	0.9540 \pm 0.0219 (0.8990 - 0.9828)	0.5021 \pm 0.1639 (0.1557 - 0.7245)
S-convLSTM	0.1180 \pm 0.0474 (0.0573 - 0.2982)	14.9111 \pm 4.1132 (4.9149 - 21.5393)	0.0798 \pm 0.0384 (0.0378 - 0.2131)	0.9289 \pm 1.4284 (0.1472 - 10.5453)	0.9547 \pm 0.0212 (0.9010 - 0.9832)	0.5141 \pm 0.1524 (0.2156 - 0.7644)
B-LSTM	0.1186 \pm 0.0488 (0.0552 - 0.3039)	15.2877 \pm 3.6730 (6.5119 - 21.3882)	0.0797 \pm 0.0389 (0.0375 - 0.2159)	1.0814 \pm 2.3849 (0.1353 - 18.0843)	0.9539 \pm 0.0221 (0.8997 - 0.9829)	0.4963 \pm 0.1587 (0.1295 - 0.7371)
B-convLSTM	0.1171 \pm 0.0476 (0.0547 - 0.2994)	14.4556 \pm 4.3182 (4.4162 - 21.2903)	0.0792 \pm 0.0383 (0.0375 - 0.2122)	0.8690 \pm 1.0808 (0.1521 - 7.6837)	0.9541 \pm 0.0223 (0.8970 - 0.9832)	0.5059 \pm 0.1539 (0.1538 - 0.7691)

model is able to estimate the displacements in parallel. Although the multi-frame Voxelmorph model had the lowest inference time and number of parameters, the motion correction performance was significantly worse than that of the proposed B-convLSTM (Table 2). In contrast, while there were no further significant differences ($p > 0.05$) between the motion correction results of S-convLSTM and B-convLSTM, the time consumption of B-convLSTM was 11.9% lower than that of S-convLSTM with similar model size. Finally, the time consumption of B-convLSTM is only 61% of the B-LSTM model with considerably reduced model size, showing that in addition to better utilizing spatial-temporal information, another advantage of the bottleneck convolutional LSTM layer is significantly reducing the time and memory consumption.

Since the BIS motion correction for each pair of frames were run in parallel, we also measured the overall compute time for a fair comparison. The total compute time includes the spatial transformation time and the upsampling time for the models under the downsampled resolution in addition to the motion estimation inference time. With the displacement field upsampling

and spatial warping, the overall compute time of B-convLSTM is ~ 65.5 min per subject (4.65 min per frame), which is still ~ 12 times faster than the fully parallelized original resolution BIS running 14 jobs in parallel (~ 13.3 hr). Without the parallel compute resource, the original BIS would take ~ 1 week and the downsampled BIS would need ~ 7.3 hours to process one subject, showing the great advantage of the savings in compute time for B-convLSTM.

3.3. ROI analysis and malignancy classification

The K_i statistics of the benign and malignant ROIs was listed in Table 4. All the motion correction methods suggested the general trend of reducing the mean and maximum K_i values while increasing the standard deviation of K_i in each ROI, which matches with the motion impact found in the simulation results as shown in Supplementary Table S1. The deep learning motion correction results further enhanced this impact compared with BIS, and the two convolutional LSTM networks showed similar amount of substantial change.

The AUCs of all the machine learning classifiers trained for

Table 3. The inference time of motion estimation and the model size comparison.

	Motion estimation inference time of one subject (second)	Trainable parameters
BIS	48034	–
BIS downsampled	1813	–
Voxelmorph	642	327,331
Voxelmorph multi-frame	101	327,331
S-convLSTM	118	501,571
B-LSTM	170	138,744,355
B-convLSTM	104	548,643

hypermetabolic ROI malignancy classification from local K_i statistics was summarized in Table 5. The average of the four (two linear and two non-linear) machine learning algorithms was also computed to assess the overall ability of distinguishing benign/malignant ROIs based on the K_i statistics. The B-convLSTM model reached the highest average AUC with lowest standard deviation and performed best for two of the four learning methods, indicating the improved classification capability compared to other motion correction methods. Note that the ROI group is relatively small and imbalanced since all the hotspots were chosen in the cancer subjects by the physician and some of those were later categorized as benign. The average ROC curve of each inter-frame motion correction method was plotted in Supplementary Figure S2, where the curve of the B-convLSTM model exceeded that of all the other motion correction methods.

The sample hypermetabolic ROI K_i images are displayed in Figure 5. The proposed inter-frame motion correction provided additional location, edge and texture changes compared to other baselines. For the lesion of esophageal adenocarcinoma (Figure 5 upper), the small artifact-like hotspot above the major lesion had a lower peak after the BIS correction, and the proposed B-convLSTM model further reduced its shape and values, in addition to sharpening and enhancing the edge of the lesion. The effect on motion-related artifacts also matches with the tumor simulation results in Supplementary Figure S2. For the metastatic melanoma lesion (Figure 5 lower), the traditional baseline BIS reduced the peaks of the hot spots and amplified the tumor texture. However, the Voxelmorph deep learning baseline increased the brightness of the originally strongest hot spot. After the motion correction of the B-convLSTM model, the estimations of peak K_i values further decreased compared to BIS. The visual differences after the proposed motion correction network might contribute to the improvement of clinical diagnosis and malignancy discrimination, although it is noted that gold standard motion-free K_i images are not available for the real patient dataset.

3.4. Hyperparameter sensitivity test

A sensitivity test was run to test the impact of regularization term lambda on the displacement field local discontinuity. According to Table 6, $\lambda = 1$ gives the lowest NFE while $\lambda = 0.1$ reaches the highest K_i/V_b NMI and NCC. As shown in Figure 6, $\lambda = 1$ performed the best on K_i and V_b spatial overlay with the least mismatch. It's likely that the weakest penalization $\lambda = 0.1$ also matched the image noise, which caused higher intensity-based alignment but also higher NFE and more visual mismatch. With a stronger regularization ($\lambda > 1$), the model is also less effective in motion estimation. The optimal λ was set to 1, consistent with the suggestions from the original Voxelmorph study (Balakrishnan et al., 2019).

4. Discussion

In this work, we proposed the usage of convolutional LSTM integrated into a deep convolutional network for fast inter-frame motion correction in dynamic PET and parametric imaging. The network allows the model to "see" multiple dynamic image series as the input together and process the spatial-temporal information and features. Compared to traditional and deep learning baselines, the proposed method successfully further enhanced the spatial alignment of the parametric K_i and V_b images and reduced inter-frame mismatch. The Patlak NFE was significantly reduced in the whole-body and head and ROI sub-areas, which exhibited considerable motion. The further modifications of the ROI appearances were observed with greater texture and shape change, and the potential of further improving the benign/malignant classification capacity following motion correction with our B-convLSTM model was suggested. Once trained, it takes ~ 4.65 min/frame to apply the proposed motion correction model, substantially reducing the time consumption compared with the traditional BIS method (~ 13.3 hr/frame).

A major obstacle holding back the clinical application of BIS motion correction is the needed long computing time. Using downsampled dynamic frames as the input was able to speed up the process (~ 31 min/frame), but the registration performance also degraded due to the lower resolution. Due to the memory limitation, the proposed motion correction network was inputted with the downsampled dynamic frame series, and the results computed based on a lower resolution still achieved greater qualitative and quantitative performances than the full-resolution BIS. The length of the input frame sequences for the proposed model was fixed at 5, which was limited by the GPU memory resource, although the high memory and computational resource requirement are from the 4-D whole-body data. Therefore, the network has the potential to be extended for longer time sequences with lower resolution such as cardiac motion tracking/prediction.

Compared to the deep learning baseline Voxelmorph with one single image pair, the Voxelmorph multi-frame showed that it is promising to have sequential inputs and the multiple frame pair registration for the dynamic PET images with related inter-frame kinetic information. We then demonstrated the advantage of integrating an LSTM layer into the multiple frame network by experimenting with three models: S-convLSTM,

Table 4. K_i statistics of the benign and malignant ROI groups for each inter-frame motion correction method (mean \pm standard deviation, range)

	Benign (n = 8)			Malignant (n = 49)		
	Mean	Maximum	Standard deviation	Mean	Maximum	Standard deviation
Without correction	0.0050 \pm 0.0028 (0.0017 - 0.0107)	0.0083 \pm 0.0044 (0.0024 - 0.0173)	0.0015 \pm 0.0007 (0.0003 - 0.0027)	0.0138 \pm 0.0079 (0.0009 - 0.0392)	0.0288 \pm 0.0192 (0.0017 - 0.0835)	0.0051 \pm 0.0036 (0.0002 - 0.0142)
BIS	0.0049 \pm 0.0028 (0.0016 - 0.0108)	0.0083 \pm 0.0046 (0.0022 - 0.0181)	0.0014 \pm 0.0007 (0.0003 - 0.0025)	0.0134 \pm 0.0077 (0.0010 - 0.0383)	0.0287 \pm 0.0187 (0.0018 - 0.0770)	0.0053 \pm 0.0037 (0.0002 - 0.0141)
BIS downsampled	0.0049 \pm 0.0028 (0.0016 - 0.0110)	0.0082 \pm 0.0045 (0.0023 - 0.0179)	0.0015 \pm 0.0007 (0.0003 - 0.0026)	0.0132 \pm 0.0078 (0.0008 - 0.0368)	0.0283 \pm 0.0186 (0.0019 - 0.0758)	0.0052 \pm 0.0037 (0.0002 - 0.0140)
Voxelmorph	0.0043 \pm 0.0031 (0.0011 - 0.0116)	0.0076 \pm 0.0045 (0.0019 - 0.0173)	0.0015 \pm 0.0007 (0.0003 - 0.0025)	0.0119 \pm 0.0074 (0.0010 - 0.0382)	0.0271 \pm 0.0183 (0.0015 - 0.0827)	0.0053 \pm 0.0039 (0.0003 - 0.0159)
Voxelmorph multi-frame	0.0047 \pm 0.0024 (0.0013 - 0.0094)	0.0082 \pm 0.0045 (0.0018 - 0.0168)	0.0017 \pm 0.0009 (0.0003 - 0.0031)	0.0116 \pm 0.0071 (0.0003 - 0.0344)	0.0276 \pm 0.0186 (0.0012 - 0.0743)	0.0055 \pm 0.0039 (0.0001 - 0.0150)
S-convLSTM	0.0041 \pm 0.0027 (0.0008 - 0.0101)	0.0076 \pm 0.0044 (0.0015 - 0.0171)	0.0014 \pm 0.0007 (0.0003 - 0.0028)	0.0118 \pm 0.0070 (0.0008 - 0.0338)	0.0276 \pm 0.0186 (0.0013 - 0.0734)	0.0055 \pm 0.0039 (0.0002 - 0.0154)
B-LSTM	0.0039 \pm 0.0021 (0.0014 - 0.0087)	0.0075 \pm 0.0045 (0.0021 - 0.0172)	0.0017 \pm 0.0010 (0.0003 - 0.0033)	0.0115 \pm 0.0067 (0.0007 - 0.0333)	0.0275 \pm 0.0187 (0.0012 - 0.0725)	0.0056 \pm 0.0041 (0.0002 - 0.0158)
B-convLSTM	0.0041 \pm 0.0024 (0.0009 - 0.0091)	0.0075 \pm 0.0045 (0.0013 - 0.0172)	0.0015 \pm 0.0010 (0.0002 - 0.0033)	0.0118 \pm 0.0068 (0.0003 - 0.0335)	0.0277 \pm 0.0183 (0.0009 - 0.0742)	0.0054 \pm 0.0039 (0.0002 - 0.0156)

Table 5. The AUCs of all the machine learning ROI malignancy classifiers for each motion correction method (mean \pm standard deviation)

	SVC	SVC Linear	RF	LR	Average
Without correction	0.8500 \pm 0.1483	0.8500 \pm 0.1483	0.6856 \pm 0.2855	0.8500 \pm 0.1483	0.8008 \pm 0.2151
BIS	0.8900 \pm 0.1114	0.8700 \pm 0.1166	0.6906 \pm 0.2669	0.8700 \pm 0.1166	0.8264 \pm 0.2018
BIS downsampled	0.8600 \pm 0.1200	0.8900 \pm 0.1114	0.7578 \pm 0.2486	0.8900 \pm 0.1114	0.8519 \pm 0.1599
Voxelmorph	0.8100 \pm 0.1855	0.8300 \pm 0.1833	0.7317 \pm 0.2172	0.8300 \pm 0.1833	0.8004 \pm 0.1971
Voxelmorph multi-frame	0.8700 \pm 0.1470	0.8500 \pm 0.1483	0.8428 \pm 0.1427	0.8500 \pm 0.1483	0.8532 \pm 0.1470
S-convLSTM	0.8478 \pm 0.1086	0.8878 \pm 0.0661	0.8528 \pm 0.1045	0.8878 \pm 0.0661	0.8640 \pm 0.0982
B-LSTM	0.8589 \pm 0.1059	0.8589 \pm 0.1059	0.9228 \pm 0.0404	0.8589 \pm 0.1059	0.8719 \pm 0.0998
B-convLSTM	0.8789 \pm 0.1022	0.9100 \pm 0.0800	0.9100 \pm 0.1114	0.9100 \pm 0.0800	0.9022 \pm 0.0954

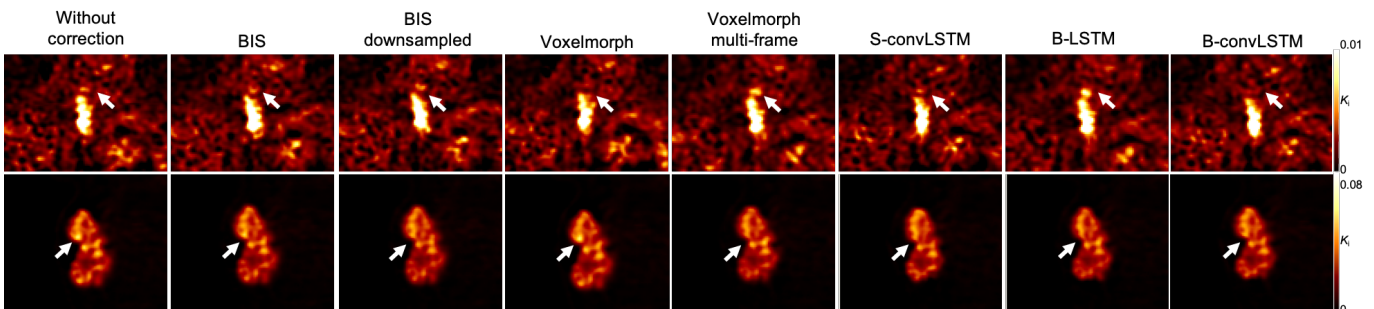
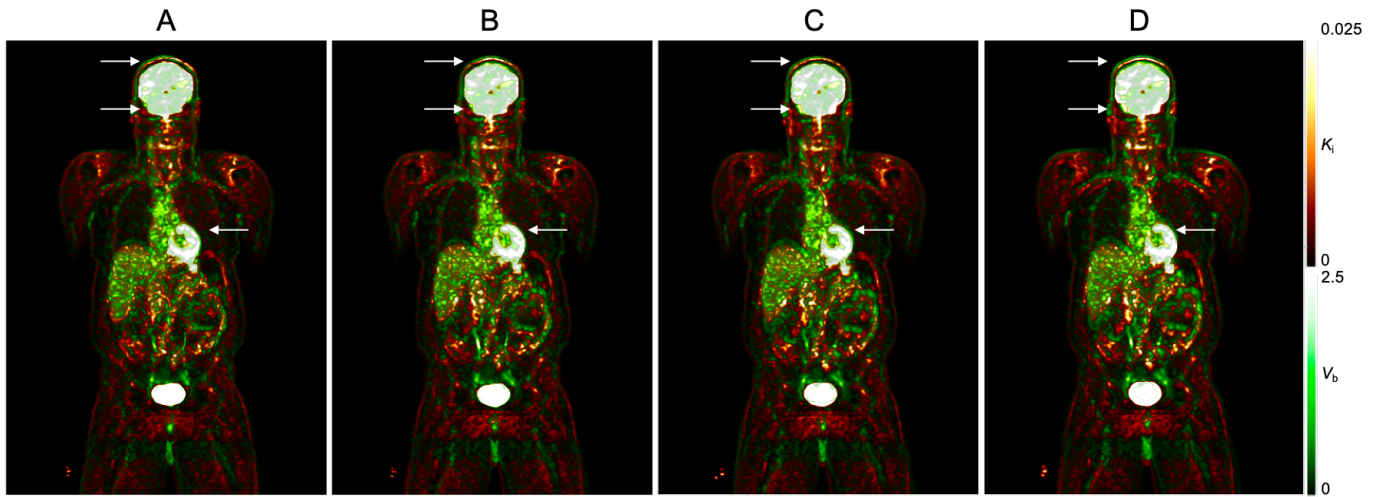
**Fig. 5.** Sample hypermetabolic ROI K_i images after each inter-frame motion correction method.

Table 6. Quantitative assessments of the sensitivity test (mean \pm standard deviation, range)

	Whole-body mean NFE	Whole-body maximum NFE	Head NFE	ROI NFE	K_i/V_b NMI	K_i/V_b NCC
$\lambda = 0.1$	0.1183 ± 0.0480 (0.0567 - 0.3067)	15.4661 ± 4.0306 (4.5706 - 21.3611)	0.0832 ± 0.0387 (0.0394 - 0.2187)	1.0495 ± 2.0207 (0.1789 - 15.2915)	0.9561 ± 0.0211 (0.9017 - 0.9839)	0.5198 ± 0.1626 (0.1866 - 0.8033)
$\lambda = 1$	0.1171 ± 0.0476 (0.0547 - 0.2994)	14.4556 ± 4.3182 (4.4162 - 21.2903)	0.0792 ± 0.0383 (0.0375 - 0.2122)	0.8690 ± 1.0808 (0.1521 - 7.6837)	0.9541 ± 0.0223 (0.8970 - 0.9832)	0.5059 ± 0.1539 (0.1538 - 0.7691)
$\lambda = 10$	0.1239 ± 0.0523 (0.0576 - 0.3188)	14.5822 ± 4.4000 (4.2601 - 21.6528)	0.0821 ± 0.0391 (0.0380 - 0.2160)	1.0364 ± 1.8285 (0.1373 - 13.8209)	0.9492 ± 0.0237 (0.8930 - 0.9820)	0.4384 ± 0.1408 (0.1547 - 0.7410)
$\lambda = 100$	0.1342 ± 0.0576 (0.0644 - 0.3466)	15.0293 ± 4.4169 (6.9871 - 21.9813)	0.0906 ± 0.0434 (0.0410 - 0.2311)	1.0449 ± 1.2975 (0.1917 - 9.1753)	0.9395 ± 0.0275 (0.8724 - 0.9784)	0.3182 ± 0.1101 (0.1094 - 0.5402)

**Fig. 6. The sample overlaid K_i (red) / V_b (green) images of the sensitivity test. (A) $\lambda = 0.1$; (B) $\lambda = 1$; (C) $\lambda = 10$; (D) $\lambda = 100$.**

with a convolutional LSTM layer serially following the multi-frame Voxelmorph network; B-LSTM, with a standard fully-connected LSTM layer implemented at the bottleneck of the U-net in the multi-frame Voxelmorph network; and our proposed B-convLSTM, with a convolutional LSTM layer integrated into the bottleneck of the U-net. The input feature map size for models with sequential connections is considerably larger than the bottleneck integration, making an S-LSTM (serial fully connected LSTM following the U-Net output) intractable, and thus only B-LSTM was tested. Compared with the fully connected LSTM, the convolutional LSTM showed its superiority in extracting spatial and temporal information simultaneously from the 4-D image series while also saving the computation and memory resources. The two ways of integrating the convolutional LSTM layer, i.e., S-convLSTM and B-convLSTM, both showed advantages in some aspects. While S-convLSTM reached the closest K_i/V_b alignment, the B-convLSTM model achieved the lowest Patlak fitting error with less soft tissue shape distortion and produced K_i estimates that resulted in the greatest ability to distinguish tumor malignancy. Moreover, With the smaller input and output feature map size, the B-convLSTM model is more practical in actual implementation with less GPU memory exhaustion.

Since the motion-free gold standard dynamic images are not available for the real dataset, the motion impact on Patlak im-

ages was evaluated by running a significant motion simulation on a tumor phantom with pseudo local shift and expansion/contraction. As shown in the supplemental material, motion introduces overestimation of K_i . Thus, motion correction is expected to generate lower K_i values in the lesion, which is consistent with our human study results presented in this paper.

There are several limitations in this work, leading to further investigations. First, our current work focuses on the inter-frame motion that causes inter-frame mismatch, including the long-term respiratory and cardiac motion pattern change and the voluntary body movement. However, the intra-frame respiratory, cardiac, and body motion could also degrade the reconstructed image quality and lead to blur, introducing quantification error in parametric imaging as well. A potential future direction is combining the inter-frame and intra-frame motion correction, which is expected to further reduce the parametric fitting error. Given that the time and computation consumption of the current intra-frame motion correction method is very high (Mohy-ud Din et al., 2015), it will be worth investigating a deep learning approach and building a joint intra-inter-frame motion correction network. Second, the current proposed network only considers the inter-frame motion correction problem, and the target parametric estimation is then separately implemented by Patlak fitting. To fully take advantage of the tracer kinetics and the inter-frame temporal dependence, future work could include

joint parametric imaging with the inter-frame motion correction to directly optimize the Patlak fitting error. Such an end-to-end framework would be more efficient and convenient for potential clinical applications. Lastly, all the current evaluations are based on a real dataset where there is no motion-free ground truth. By running motion simulations on generated motion-free phantoms, the motion correction performance would be more quantitatively evaluated.

In addition to the current limitations, some potential future directions are worth investigating. With other datasets under different tracers/imaging protocols, we could test the robustness of the proposed motion correction model. Transfer learning could also be applied for the model to generalize across different tracers, scanners, and imaging protocols. Also, the attention mechanism (Vaswani *et al.*, 2017) has been proposed in natural language processing and shown its superiority in video capturing (Cai and Wei, 2020) and CT image segmentation (Oktay *et al.*, 2018). Introducing the attention mechanism into our motion correction model may help further correct the subareas with significant motion and improve the model performance. Finally, the backbone of the network is interchangeable and not limited to the U-Net used in this work. For example, Transformer based models have been widely used in a variety of natural language tasks (Gillioz *et al.*, 2020), and has been recently reported in image generation (Parmar *et al.*, 2018) and image restoration (Wang *et al.*, 2021b). It is worth investigating various backbone structures and further improve the model performance and efficiency.

5. Conclusion

In this work, we presented a new deep learning inter-frame motion correction method for dynamic PET and parametric imaging. Our proposed model integrated a convolutional LSTM layer into the bottleneck of a U-net style convolutional network to estimate motion across multiple dynamic PET frames. Compared with both traditional and deep learning baseline methods, the proposed convolutional LSTM model successfully further reduced the Patlak NFE and enhanced spatial alignment of the Patlak K_i and V_b images. In hypermetabolic ROIs, notable additional K_i value changes and tumor texture changes were observed, with improved benign/malignant classification capability after correcting for motion with our proposed model. The well-trained network could perform motion estimation at around 7.4 seconds per frame, and the entire motion correction pipeline consumed only 1/12 of the wall time for the fully parallelized traditional BIS method and 1/170 of the overall compute time for BIS. Our proposed methods demonstrate the potential of introducing multiple-frame analysis and extracting spatial and temporal information for correcting motion in dynamic PET images.

Acknowledgments

This work was under the support of the National Institutes of Health (NIH) through grant R01 CA224140 and a research contract from Siemens Medical Solutions USA, Inc.

Bruce Spottiswoode, David Pigg and Michael E. Casey are employees of Siemens Medical Solutions USA, Inc. No other potential conflicts of interest relevant to this article exist.

References

- Abdi, A.H., Luong, C., Tsang, T., Jue, J., Gin, K., Yeung, D., Hawley, D., Rohling, R., Abolmaesumi, P., 2017. Quality assessment of echocardiographic cine using recurrent neural networks: Feasibility on five standard view planes, in: International Conference on Medical Image Computing and Computer-Assisted Intervention, Springer. pp. 302–310.
- Arbelle, A., Raviv, T.R., 2019. Microscopy cell segmentation via convolutional lstm networks, in: 2019 IEEE 16th International Symposium on Biomedical Imaging (ISBI 2019), IEEE. pp. 1008–1012.
- Azad, R., Asadi-Aghbolaghi, M., Fathy, M., Escalera, S., 2019. Bi-directional convlstm u-net with densely connected convolutions, in: Proceedings of the IEEE/CVF International Conference on Computer Vision Workshops, pp. 0–0.
- Azizmohammadi, F., Martin, R., Miro, J., Duong, L., 2019. Model-free cardiorespiratory motion prediction from x-ray angiography sequence with lstm network, in: 2019 41st Annual International Conference of the IEEE Engineering in Medicine and Biology Society (EMBC), IEEE. pp. 7014–7018.
- Balakrishnan, G., Zhao, A., Sabuncu, M.R., Guttag, J., Dalca, A.V., 2019. Voxelmorph: a learning framework for deformable medical image registration. *IEEE transactions on medical imaging* 38, 1788–1800.
- Cai, W., Wei, Z., 2020. Remote sensing image classification based on a cross-attention mechanism and graph convolution. *IEEE Geoscience and Remote Sensing Letters*.
- Carson, R.E., 2005. Tracer kinetic modeling in pet, in: Positron Emission Tomography. Springer, pp. 127–159.
- Chen, J., Yang, L., Zhang, Y., Alber, M., Chen, D.Z., 2016. Combining fully convolutional and recurrent neural networks for 3d biomedical image segmentation, in: Advances in neural information processing systems, pp. 3036–3044.
- Chen, K., Huang, S.C., Yu, D.C., 1991. The effects of measurement errors in the plasma radioactivity curve on parameter estimation in positron emission tomography. *Physics in Medicine & Biology* 36, 1183.
- Chen, K., Reiman, E., Lawson, M., Feng, D., Huang, S.C., 1995. Decay correction methods in dynamic pet studies. *IEEE Transactions on nuclear science* 42, 2173–2179.
- Çiçek, Ö., Abdulkadir, A., Lienkamp, S.S., Brox, T., Ronneberger, O., 2016. 3d u-net: learning dense volumetric segmentation from sparse annotation, in: International conference on medical image computing and computer-assisted intervention, Springer. pp. 424–432.
- Dimitrakopoulou-Strauss, A., Pan, L., Sachpekidis, C., 2021. Kinetic modeling and parametric imaging with dynamic pet for oncological applications: General considerations, current clinical applications, and future perspectives. *European Journal of Nuclear Medicine and Molecular Imaging* 48, 21–39.
- Mohy-ud Din, H., Nicolas, A., Willis, W., Abdel, K., Dean, F., Rahmim, A., *et al.*, 2015. Intra-frame motion compensation in multi-frame brain pet imaging. *Frontiers in Biomedical Technologies* 2, 60–72.
- Fahrni, G., Karakatsanis, N.A., Di Domenicantonio, G., Garibotto, V., Zaidi, H., 2019. Does whole-body patlak 18 f-fdg pet imaging improve lesion detectability in clinical oncology? *European radiology* 29, 4812–4821.
- Feng, T., Wang, J., Sun, Y., Zhu, W., Dong, Y., Li, H., 2017. Self-gating: an adaptive center-of-mass approach for respiratory gating in pet. *IEEE transactions on medical imaging* 37, 1140–1148.
- Gallezot, J.D., Lu, Y., Naganawa, M., Carson, R.E., 2019. Parametric imaging with pet and spect. *IEEE Transactions on Radiation and Plasma Medical Sciences* 4, 1–23.
- Ge, H., Yan, Z., Yu, W., Sun, L., 2019. An attention mechanism based convolutional lstm network for video action recognition. *Multimedia Tools and Applications* 78, 20533–20556.
- Gillioz, A., Casas, J., Mugellini, E., Abou Khaled, O., 2020. Overview of the transformer-based models for nlp tasks, in: 2020 15th Conference on Computer Science and Information Systems (FedCSIS), IEEE. pp. 179–183.
- Guo, X., Wu, J., Chen, M.K., Onofrey, J., Pang, Y., Pigg, D., Casey, M., Dvornek, N., Liu, C., 2021. Inter-pass motion correction for whole-body dynamic parametric pet imaging.

- Guo, Y., Dvornek, N., Lu, Y., Tsai, Y.J., Hamill, J., Casey, M., Liu, C., 2019. Deep learning based respiratory pattern classification and applications in pet/ct motion correction, in: 2019 IEEE Nuclear Science Symposium and Medical Imaging Conference (NSS/MIC), IEEE. pp. 1–5.
- Hanson, A., Pnvr, K., Krishnagopal, S., Davis, L., 2018. Bidirectional convolutional lstm for the detection of violence in videos, in: Proceedings of the European Conference on Computer Vision (ECCV) Workshops, pp. 0–0.
- Hochreiter, S., Schmidhuber, J., 1997. Long short-term memory. *Neural computation* 9, 1735–1780.
- Huang, W., Bridge, C.P., Noble, J.A., Zisserman, A., 2017. Temporal heartnet: towards human-level automatic analysis of fetal cardiac screening video, in: International Conference on Medical Image Computing and Computer-Assisted Intervention, Springer. pp. 341–349.
- Hudson, H.M., Larkin, R.S., 1994. Accelerated image reconstruction using ordered subsets of projection data. *IEEE transactions on medical imaging* 13, 601–609.
- Joshi, A., Scheinost, D., Okuda, H., Belhachemi, D., Murphy, I., Staib, L.H., Papademetris, X., 2011. Unified framework for development, deployment and robust testing of neuroimaging algorithms. *Neuroinformatics* 9, 69–84.
- Karakatsanis, N.A., Lodge, M.A., Tahari, A.K., Zhou, Y., Wahl, R.L., Rahmim, A., 2013. Dynamic whole-body pet parametric imaging: I. concept, acquisition protocol optimization and clinical application. *Physics in Medicine & Biology* 58, 7391.
- Lu, Y., Fontaine, K., Mulnix, T., Onofrey, J.A., Ren, S., Panin, V., Jones, J., Casey, M.E., Barnett, R., Kench, P., et al., 2018. Respiratory motion compensation for pet/ct with motion information derived from matched attenuation-corrected gated pet data. *Journal of nuclear Medicine* 59, 1480–1486.
- Lu, Y., Gallezot, J.D., Naganawa, M., Ren, S., Fontaine, K., Wu, J., Onofrey, J.A., Toyonaga, T., Boutagy, N., Mulnix, T., et al., 2019. Data-driven voluntary body motion detection and non-rigid event-by-event correction for static and dynamic pet. *Physics in Medicine & Biology* 64, 065002.
- Lu, Y., Naganawa, M., Toyonaga, T., Gallezot, J.D., Fontaine, K., Ren, S., Revilla, E.M., Mulnix, T., Carson, R.E., 2020. Data-driven motion detection and event-by-event correction for brain pet: Comparison with vicra. *Journal of Nuclear Medicine* 61, 1397–1403.
- Medsker, L.R., Jain, L., 2001. Recurrent neural networks. *Design and Applications* 5.
- Merity, S., Keskar, N.S., Socher, R., 2017. Regularizing and optimizing lstm language models. *arXiv preprint arXiv:1708.02182*.
- Muzi, M., O'Sullivan, F., Mankoff, D.A., Doot, R.K., Pierce, L.A., Kurland, B.F., Linden, H.M., Kinahan, P.E., 2012. Quantitative assessment of dynamic pet imaging data in cancer imaging. *Magnetic resonance imaging* 30, 1203–1215.
- Naganawa, M., Gallezot, J.D., Shah, V., Mulnix, T., Young, C., Dias, M., Chen, M.K., Smith, A.M., Carson, R.E., 2020. Assessment of population-based input functions for patlak imaging of whole body dynamic 18 f-fdg pet. *EJN-MMI physics* 7, 1–15.
- Noonan, P., Howard, J., Hallett, W., Gunn, R., 2015. Repurposing the microsoft kinect for windows v2 for external head motion tracking for brain pet. *Physics in Medicine & Biology* 60, 8753.
- Oktaç, O., Schlemper, J., Folgoc, L.L., Lee, M., Heinrich, M., Misawa, K., Mori, K., McDonagh, S., Hammerla, N.Y., Kainz, B., et al., 2018. Attention u-net: Learning where to look for the pancreas. *arXiv preprint arXiv:1804.03999*.
- Panin, V.Y., Smith, A.M., Hu, J., Kehren, F., Casey, M.E., 2014. Continuous bed motion on clinical scanner: design, data correction, and reconstruction. *Physics in Medicine & Biology* 59, 6153.
- Papadomanolaki, M., Vakalopoulou, M., Karantzas, K., 2021. A deep multitask learning framework coupling semantic segmentation and fully convolutional lstm networks for urban change detection. *IEEE Transactions on Geoscience and Remote Sensing*.
- Parmar, N., Vaswani, A., Uszkoreit, J., Kaiser, L., Shazeer, N., Ku, A., Tran, D., 2018. Image transformer, in: International Conference on Machine Learning, PMLR. pp. 4055–4064.
- Patlak, C.S., Blasberg, R.G., Fenstermacher, J.D., 1983. Graphical evaluation of blood-to-brain transfer constants from multiple-time uptake data. *Journal of Cerebral Blood Flow & Metabolism* 3, 1–7.
- Ronneberger, O., Fischer, P., Brox, T., 2015. U-net: Convolutional networks for biomedical image segmentation, in: International Conference on Medical image computing and computer-assisted intervention, Springer. pp. 234–241.
- Shi, L., Lu, Y., Dvornek, N., Weyman, C.A., Miller, E.J., Sinusas, A.J., Liu, C., 2021. Automatic inter-frame patient motion correction for dynamic cardiac pet using deep learning. *IEEE Transactions on Medical Imaging*.
- Shi, X., Chen, Z., Wang, H., Yeung, D.Y., Wong, W.K., Woo, W.c., 2015. Convolutional lstm network: A machine learning approach for precipitation nowcasting. *arXiv preprint arXiv:1506.04214*.
- Sun, S., Mu, L., Wang, L., Liu, P., 2020. L-unet: An lstm network for remote sensing image change detection. *IEEE Geoscience and Remote Sensing Letters*.
- Toczek, J., Wu, J., Hillmer, A.T., Han, J., Esterlis, I., Cosgrove, K.P., Liu, C., Sadeghi, M.M., 2020. Accuracy of arterial [18 f]-fluorodeoxyglucose uptake quantification: A kinetic modeling study. *Journal of Nuclear Cardiology*, 1–4.
- Vaswani, A., Shazeer, N., Parmar, N., Uszkoreit, J., Jones, L., Gomez, A.N., Kaiser, L., Polosukhin, I., 2017. Attention is all you need, in: Advances in neural information processing systems, pp. 5998–6008.
- Wang, G., Li, Z., Li, G., Dai, G., Xiao, Q., Bai, L., He, Y., Liu, Y., Bai, S., 2021a. Real-time liver tracking algorithm based on lstm and svr networks for use in surface-guided radiation therapy. *Radiation Oncology* 16, 1–12.
- Wang, Z., Cun, X., Bao, J., Liu, J., 2021b. Uformer: A general u-shaped transformer for image restoration. *arXiv preprint arXiv:2106.03106*.
- Wright, R., Khanal, B., Gomez, A., Skelton, E., Matthew, J., Hajnal, J.V., Rueckert, D., Schnabel, J.A., 2018. Lstm spatial co-transformer networks for registration of 3d fetal us and mr brain images, in: Data Driven Treatment Response Assessment and Preterm, Perinatal, and Paediatric Image Analysis. Springer. pp. 149–159.
- Wu, J., Kim, M., Peters, J., Chung, H., Samant, S.S., 2009. Evaluation of similarity measures for use in the intensity-based rigid 2d-3d registration for patient positioning in radiotherapy. *Medical physics* 36, 5391–5403.
- Xue, W., Brahm, G., Pandey, S., Leung, S., Li, S., 2018. Full left ventricle quantification via deep multitask relationships learning. *Medical image analysis* 43, 54–65.
- Yang, X., Kwitt, R., Styner, M., Niethammer, M., 2017. Quicksilver: Fast predictive image registration—a deep learning approach. *NeuroImage* 158, 378–396.
- Ye, Q., Wu, J., Lu, Y., Naganawa, M., Gallezot, J.D., Ma, T., Liu, Y., Tanoue, L., Deterbeck, F., Blasberg, J., et al., 2018. Improved discrimination between benign and malignant ldct screening-detected lung nodules with dynamic over static 18f-fdg pet as a function of injected dose. *Physics in Medicine & Biology* 63, 175015.
- Zeng, Q., Fu, Y., Jeong, J., Lei, Y., Wang, T., Mao, H., Jani, A.B., Patel, P., Curran, W.J., Liu, T., et al., 2020. Weakly non-rigid mr-trus prostate registration using fully convolutional and recurrent neural networks, in: Medical Imaging 2020: Image Processing, International Society for Optics and Photonics. p. 113132Y.
- Zhang, D., Icke, I., Dogdas, B., Parimal, S., Sampath, S., Forbes, J., Bagchi, A., Chin, C.L., Chen, A., 2018a. A multi-level convolutional lstm model for the segmentation of left ventricle myocardium in infarcted porcine cine mr images, in: 2018 IEEE 15th International Symposium on Biomedical Imaging (ISBI 2018), IEEE. pp. 470–473.
- Zhang, D., Icke, I., Dogdas, B., Parimal, S., Sampath, S., Forbes, J., Bagchi, A., Chin, C.L., Chen, A., 2018b. Segmentation of left ventricle myocardium in porcine cardiac cine mr images using a hybrid of fully convolutional neural networks and convolutional lstm, in: Medical Imaging 2018: Image Processing, International Society for Optics and Photonics. p. 105740A.
- Zhou, B., Tsai, Y.J., Chen, X., Duncan, J.S., Liu, C., 2021. Mdpet: A unified motion correction and denoising adversarial network for low-dose gated pet. *IEEE Transactions on Medical Imaging*.
- Zhu, G., Zhang, L., Shen, P., Song, J., 2017. Multimodal gesture recognition using 3-d convolution and convolutional lstm. *Ieee Access* 5, 4517–4524.
- Ziegler, S.I., 2005. Positron emission tomography: principles, technology, and recent developments. *Nuclear Physics A* 752, 679–687.

Supplementary Material

The significant motion simulation was run on a synthetic tumor phantom to assess the motion impact on Patlak images. The pseudo local shift and expansion/contraction were implemented for simulating both rigid and non-rigid motion with random displacement magnitudes from -100mm to 100mm. To observe the motion impact more clearly, the maximum simulated motion magnitude was larger than the real dataset. We simulated one motion-free scan and five motion simulation scans, each acquiring 19 dynamic frames. The Patlak fitting was then implemented for the motion free and five motion simulation dynamic frame series. In Supplementary Table S1, the K_i statistics and the NFE results were summarized in comparison between the motion simulations and the motion-free ground truth. In Supplementary Figure S1, the K_i image and the NFE map of a sample motion simulation and the motion-free ground truth were visualized. The sample profile of the tumor was also visualized to directly display the motion impact on Patlak K_i image.

Table S1. Patlak K_i statistics and NFE results in motion simulation (mean \pm standard deviation)

	Motion simulation	Motion-free ground truth
K_i mean	0.0193 ± 0.0034	0.0146
K_i maximum	0.0514 ± 0.0073	0.0385
NFE	8.5589 ± 0.9460	0.0187

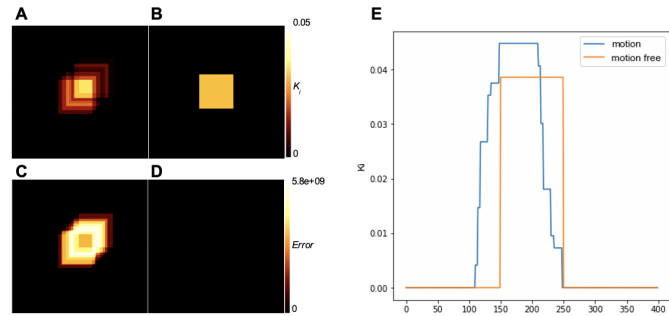


Fig. S1. Motion simulation results on a tumor phantom. (A) Sample Patlak K_i image with simulated motion; (B) Sample motion-free Patlak K_i image; (C) Sample NFE map with motion; (D) Sample motion-free NFE map; (E) Sample profile of the tumor at the middle of the slice, with motion simulation and motion free.

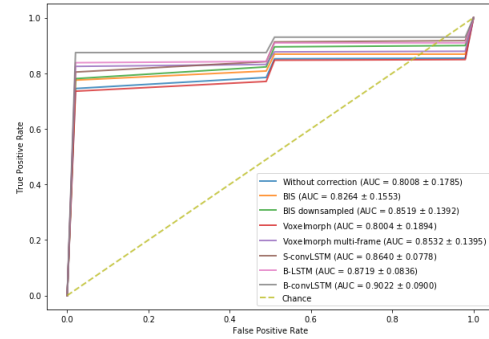


Fig. S2. The average ROC curve of each inter-frame motion correction method compared with chance. Note that due to the small number of test samples in each of the 5 folds of stratified cross-validation, the number of distinct thresholds at which a new point on the ROC is generated is also relatively low.